

# Supporting Information

## Spindle Single-Crystalline Rutile TiO<sub>2</sub> with Excellent Cyclability for Low-Cost Li-Storage Materials

*Hiroyuki Usui<sup>†,§</sup>, Yasuhiro Domi<sup>†,§</sup>, Shinya Ohnishi<sup>†,§</sup>, Noriyuki Takamori<sup>†,§</sup>, Shin-ichiro Izaki<sup>†,§</sup>,  
Naoki Morimoto<sup>||</sup>, Kazumi Yamanaka<sup>||</sup>, Keita Kobayashi<sup>||</sup>, and Hiroki Sakaguchi<sup>†,§,\*</sup>*

<sup>†</sup> Department of Chemistry and Biotechnology, Graduate School of Engineering, Tottori University, 4-101 Minami, Koyama-cho, Tottori 680-8552, Japan

<sup>\*</sup> Course of Chemistry and Biotechnology, Department of Engineering, Graduate School of Sustainability Science, Tottori University, 4-101 Minami, Koyama-cho, Tottori 680-8552, Japan

<sup>§</sup> Center for Research on Green Sustainable Chemistry, Tottori University, 4-101 Minami, Koyama-cho, Tottori 680-8552, Japan

<sup>||</sup> Corporate Research Laboratories, Research & Development Division, Sakai Chemical Industry Co., Ltd., 5-1 Ebisujima-cho, Sakai-ku, Sakai, Osaka 590-0985, Japan

\*Corresponding Author:

Tel./Fax: +81-857-31-5265, E-mail: sakaguch@tottori-u.ac.jp

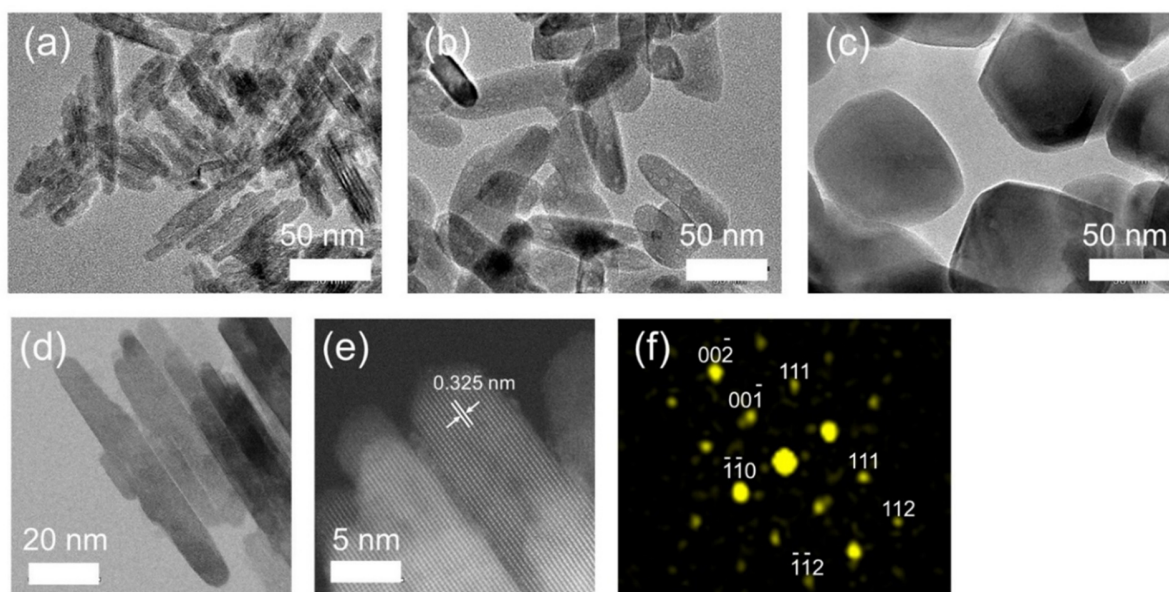


**Figure S1** TEM images of (a) spindle (without heat treatment), (b) agglomerated, and (c) sintered  $\text{TiO}_2$  particles. (d) Bright field scanning transmission electron microscopic (STEM) image of spindle  $\text{TiO}_2$  particles. (e) High-angle annular dark field STEM image spindle  $\text{TiO}_2$  particles. (f) Corresponding fast Fourier transformation pattern of (e).

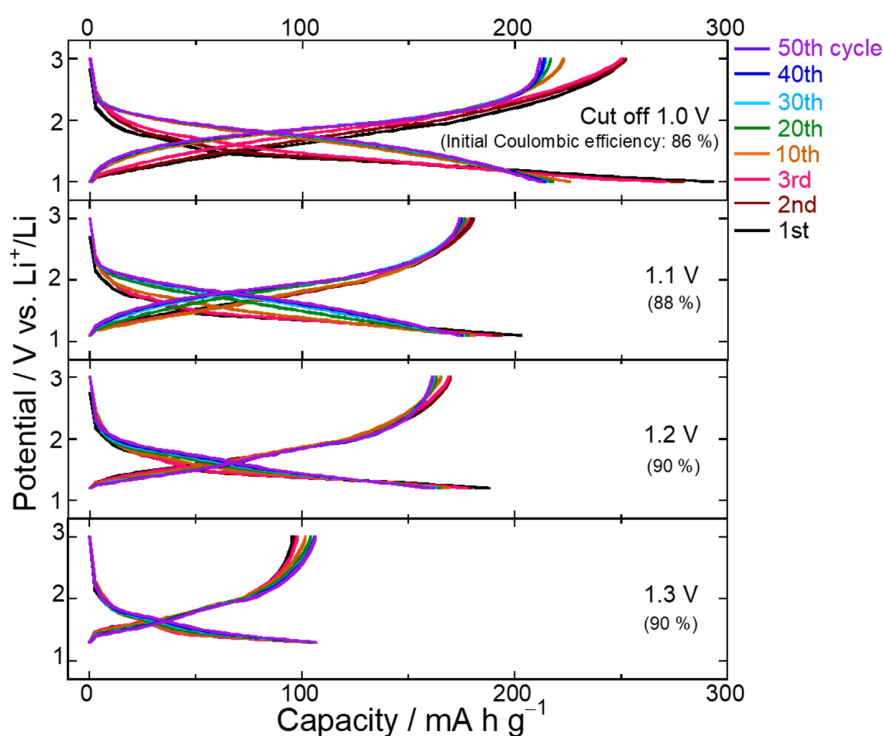


**Figure S2** Charge-discharge curves of spindle  $\text{TiO}_2$  electrodes cycled by different cut off potentials of Li-insertion. With raising the cut off potential from 1.0 to 1.2 V vs.  $\text{Li}^+/\text{Li}$ , the Coulombic efficiency can be improved though the charge-discharge capacities were reduced.

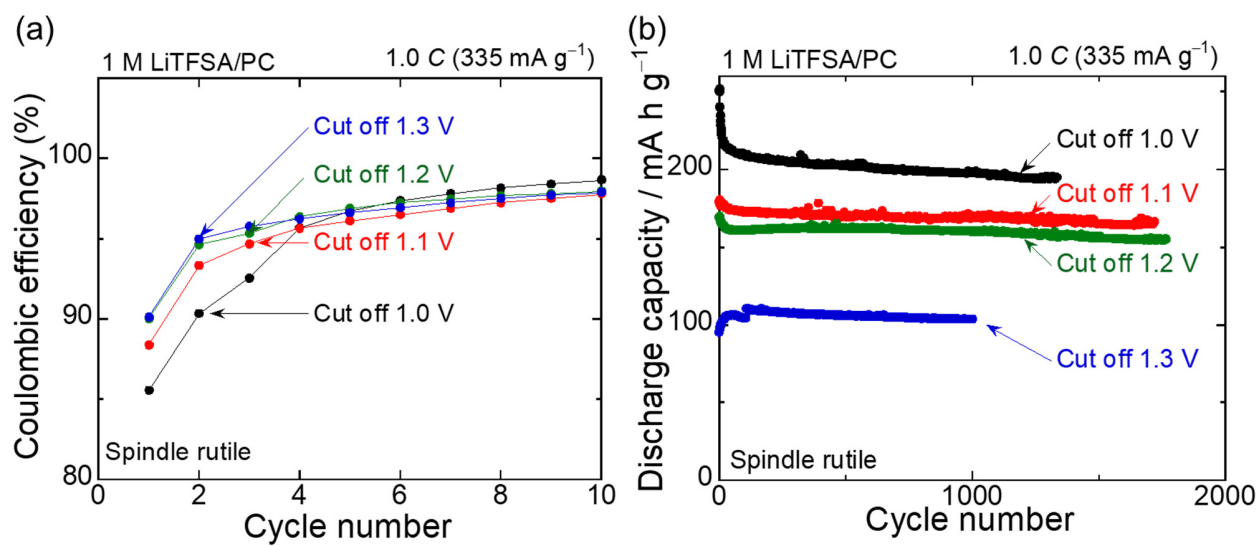


**Figure S3** (a) Changes in Coulombic efficiencies and (b) cycling performances of spindle  $\text{TiO}_2$  electrodes cycled by different cut off potentials of Li-insertion.

### ***In-situ* XRD measurement conditions**

We made a hole in the case of a 2032-type coin cell, and prepared an in-situ XRD measurement cell. As X-ray window, polyimide film was used. For good X-ray penetration, very thin Cu foil (2  $\mu\text{m}$ ) was employed as a current collector. A potentiostat (Ivium CompactStat PlusA) was used for the measurement. The cable of the potentiostat was pulled into the XRD equipment to maintain the electrode potential during XRD measurements. Charge–discharge was carried out under a constant current density of 335  $\text{mA g}^{-1}$ . At each measurement point, the electrode potential was maintained for 2000 s because one scan takes 1800 s.

#### **[In-situ XRD cell]**

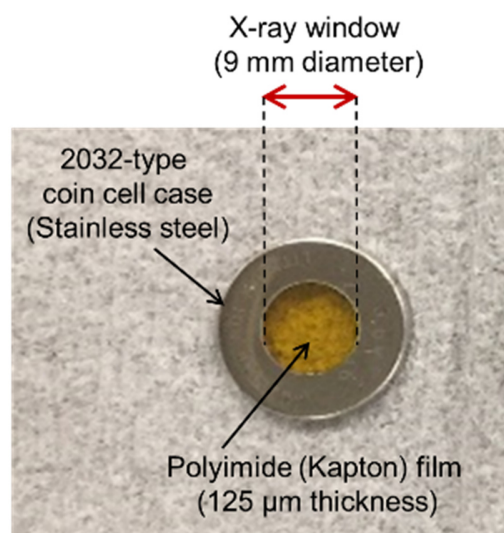
Coin cell: 2032-type (stainless steel) with 9 mm-diameter hole as X-ray window  
Current collector: Cu foil (2  $\mu\text{m}$  thickness)  
X-ray window: Polyimide film (Kapton film) (125  $\mu\text{m}$  thickness)  
Active material: Spindle  $\text{TiO}_2$  (1.0  $\text{mg cm}^{-2}$ )  
Separator: Glass fiber (250  $\mu\text{m}$  thickness)  
Electrolyte: 1 M LiTFS/PC  
Counter electrode: Li sheet (1 mm)

#### **[XRD measurement]**

XRD equipment: Rigaku Ultima IV  
X-ray:  $\text{CuK}\alpha$   
Voltage: 40 kV  
Current: 40 mA  
Scan speed: 2  $\text{deg. min}^{-1}$   
Scan range: 20–80  $\text{deg.}$   
Scan time: About 1800 s

#### **[Charge–discharge conditions]**

Equipment: Ivium CompactStatPlusA  
Current density: 335  $\text{mA g}^{-1}$  (1.0 C)  
Potential range: 1.000–3.000 V vs.  $\text{Li}^+/\text{Li}$   
Measurement point: Lithiation 1.8, 1.6, 1.2, 1.0 V vs.  $\text{Li}^+/\text{Li}$   
Delithiation 1.6, 2.2, 3.0 V vs.  $\text{Li}^+/\text{Li}$   
Keeping potential: About 2000 s for each measurement point



In the *in-situ* XRD measurement for spindle rutile  $\text{TiO}_2$  electrode, diffraction peaks of rutile  $\text{TiO}_2$  were confirmed at 27 and 54 deg. Other peaks originated from Cu foil of current collector substrate and stainless steel case of the *in-situ* coin cell. In addition, small peaks appeared at 51.5 deg. These peaks are attributed to a distorted rutile phase (monoclinic  $\text{Li}_x\text{TiO}_2$ ,  $P2/m$ ). It is suggested that these additional peaks appeared by lowering crystallographic symmetry of rutile phase. Rutile  $\text{TiO}_2$  phase can be reversibly changed to monoclinic  $\text{Li}_x\text{TiO}_2$  phase in the composition range of  $0 < x < 0.8$  (Christensen, C. K. *et al.*, *Nanoscale* **2019**, *11*, 12347.). The peak intensities of monoclinic  $\text{Li}_x\text{TiO}_2$  phase were increased by lithiation, and were decreased by delithiation. When Li was completely extracted, the peaks almost disappeared.

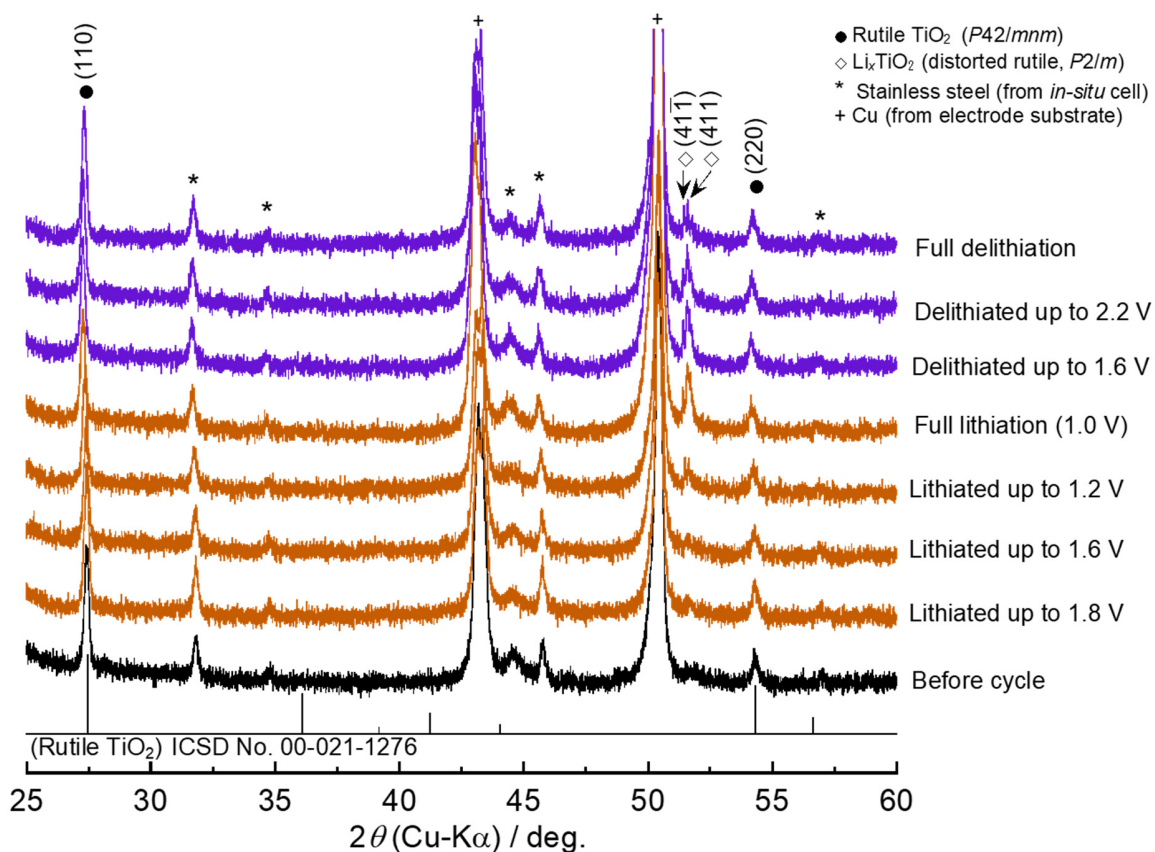


**Figure S4** Detailed results of *in-situ* XRD measurement for spindle  $\text{TiO}_2$  electrode.

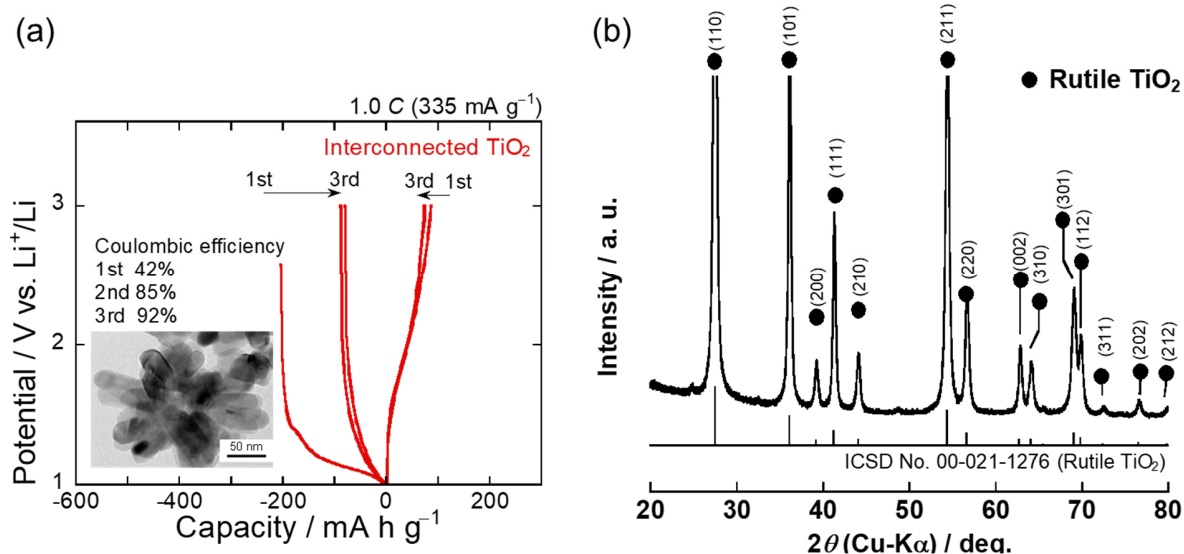


**Figure S5** (a) Constant-current charge-discharge curves of the interconnected  $\text{TiO}_2$  electrode in the initial three cycles under current density of  $335 \text{ mA g}^{-1}$  ( $1.0 \text{ C}$ ). As shown in the inset of TEM image, the particles have a structure of interconnected ellipsoidal particles. The averaged specific surface area is  $62 \text{ m}^2 \text{ g}^{-1}$ . (b) XRD pattern of the interconnected rutile  $\text{TiO}_2$  particles.

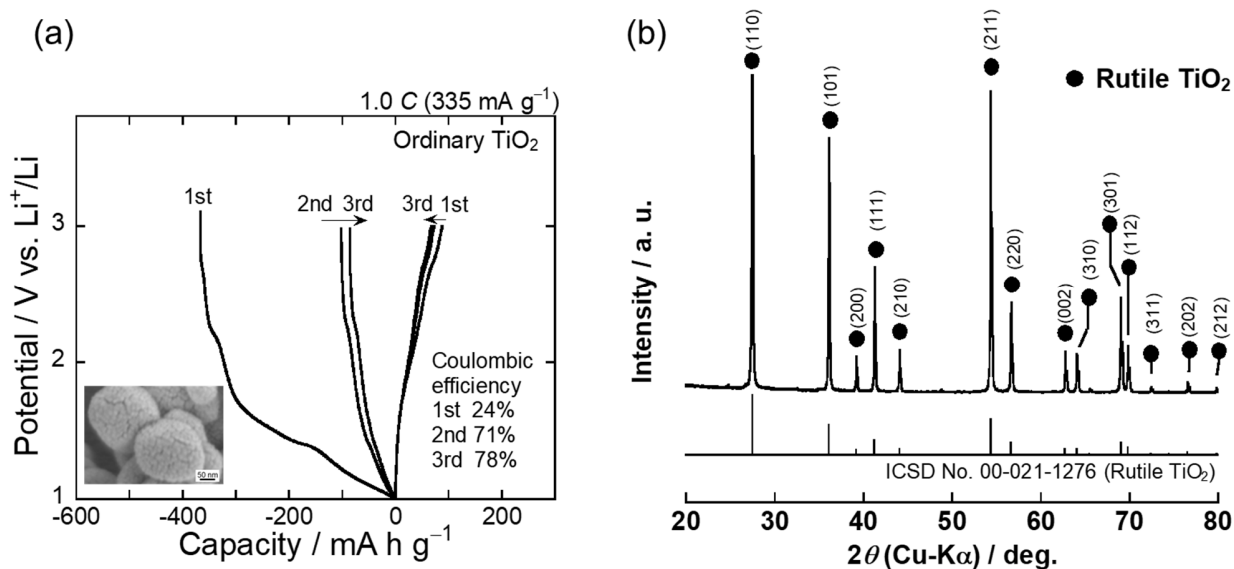


**Figure S6** (a) Constant-current charge-discharge curves of the ordinary  $\text{TiO}_2$  electrode in the initial three cycles under current density of  $335 \text{ mA g}^{-1}$  ( $1.0 \text{ C}$ ). The inset is SEM image of the particles. (b) XRD pattern of the ordinary rutile  $\text{TiO}_2$  particles.



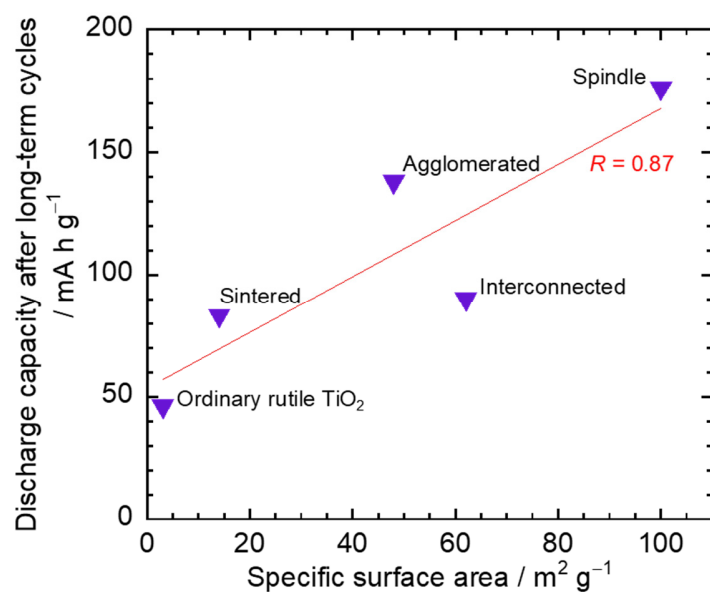


**Figure S7** Insufficient correlation between the specific surface area of rutile  $\text{TiO}_2$  particles and the discharge capacities after the capacity decays for the rutile  $\text{TiO}_2$  electrodes. The correlation coefficient  $R$  of the linear approximation was 0.87.

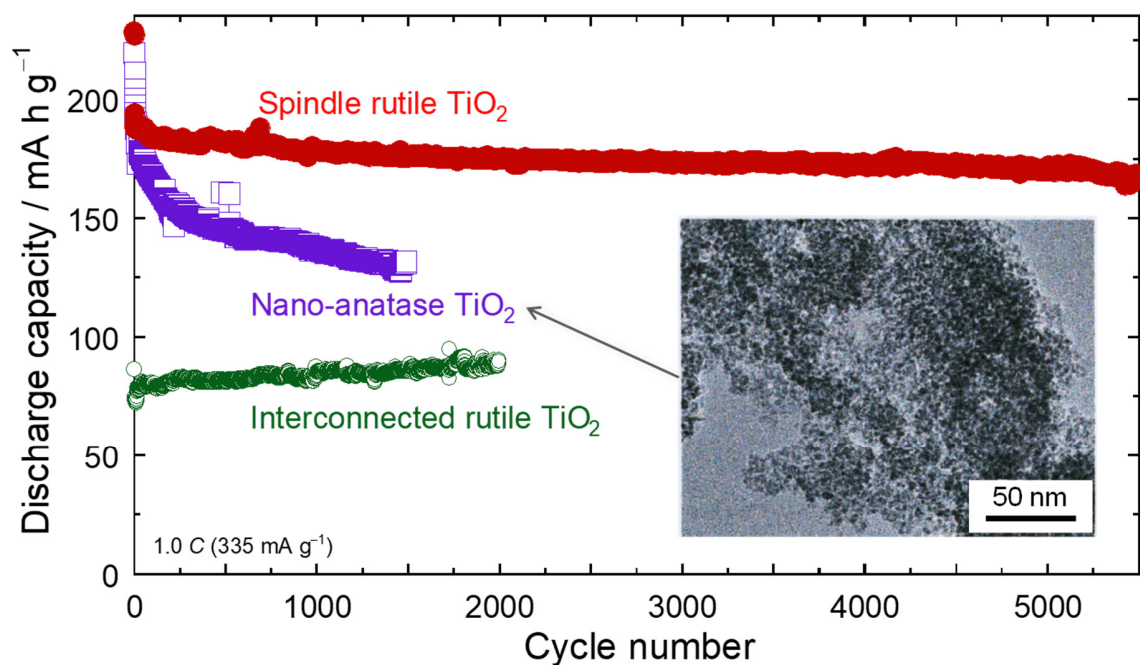


**Figure S8** Cycling performances of nano-anatase  $\text{TiO}_2$  electrode and aggregated rutile  $\text{TiO}_2$  electrodes. The inset is TEM image of nano-anatase  $\text{TiO}_2$ : very small fine particles were confirmed. The specific surface area is as large as  $313 \text{ m}^2 \text{g}^{-1}$ . For nano-anatase  $\text{TiO}_2$ , both the crystallite size and the crystallite size were 7 nm, indicating the  $R_s$  value of approximately 1.0.

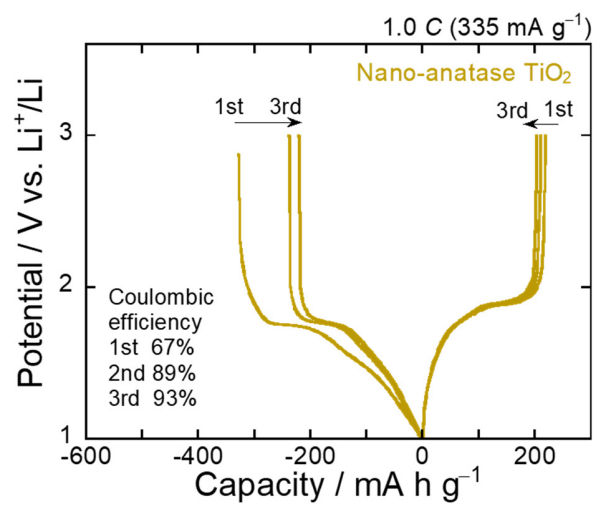


**Figure S9** Constant-current charge-discharge curves of nano-anatase TiO<sub>2</sub> electrode in the initial three cycles under current density of 335 mA g<sup>-1</sup> (1.0 C).



## The effects of Nb doping into spindle rutile TiO<sub>2</sub>

The doping of impurity elements into TiO<sub>2</sub> has been investigated for the application of transparent conductor materials. The authors have for the first time reported Nb-doped rutile TiO<sub>2</sub> for active materials of Li-storage and Na-storage (*ACS Appl. Mater. Interfaces* **2015**, 7, 6567.; *ACS Sustainable Chem. Eng.* **2016**, 4, 6695.). It has been revealed that Nb doping can improve anode properties of rutile TiO<sub>2</sub> electrodes. Thus, in this study, the Nb doping was carried out for spindle single-crystalline rutile TiO<sub>2</sub> particles by the large-scaled sulfate process.

In the sulfate process, a water-soluble niobium compound was added as Nb source into the titanyl sulfate solution. And then, thermal hydrolysis treatment was proceeded to generate Nb-doped TiO<sub>2</sub> with white color. As shown in TEM image (**Figure S10(a)**), the almost same spindle morphology was confirmed for the product prepared by adding Nb source. The particle size was also almost the same. The XRD pattern proves the single phase of rutile TiO<sub>2</sub> (**Figure S10(b)**). The peak shifts were observed for the Nb-doped TiO<sub>2</sub> particles, indicating a substitutional solid solution of Nb<sup>5+</sup> (ionic radius: 64 pm) to sites of Ti<sup>4+</sup> (60.5 pm). The X-ray fluorescent analysis detected 3 at.% Nb from the particles (**Figure S10(c)**). No significant change was found for the specific surface area and the crystallite size. The electrical resistivity was measured for the pressed powder by two probe method. The resistivity was not changed by Nb doping. On the other hand, we could confirm the doping effect for the lattice expansion: the lattice parameter of *a* was enlarged by 3 at.% Nb doping. This is very important for Li<sup>+</sup> kinetics in rutile TiO<sub>2</sub> because the size of Li<sup>+</sup> diffusion path along *c* axis is related to the lattice parameter of *a*.

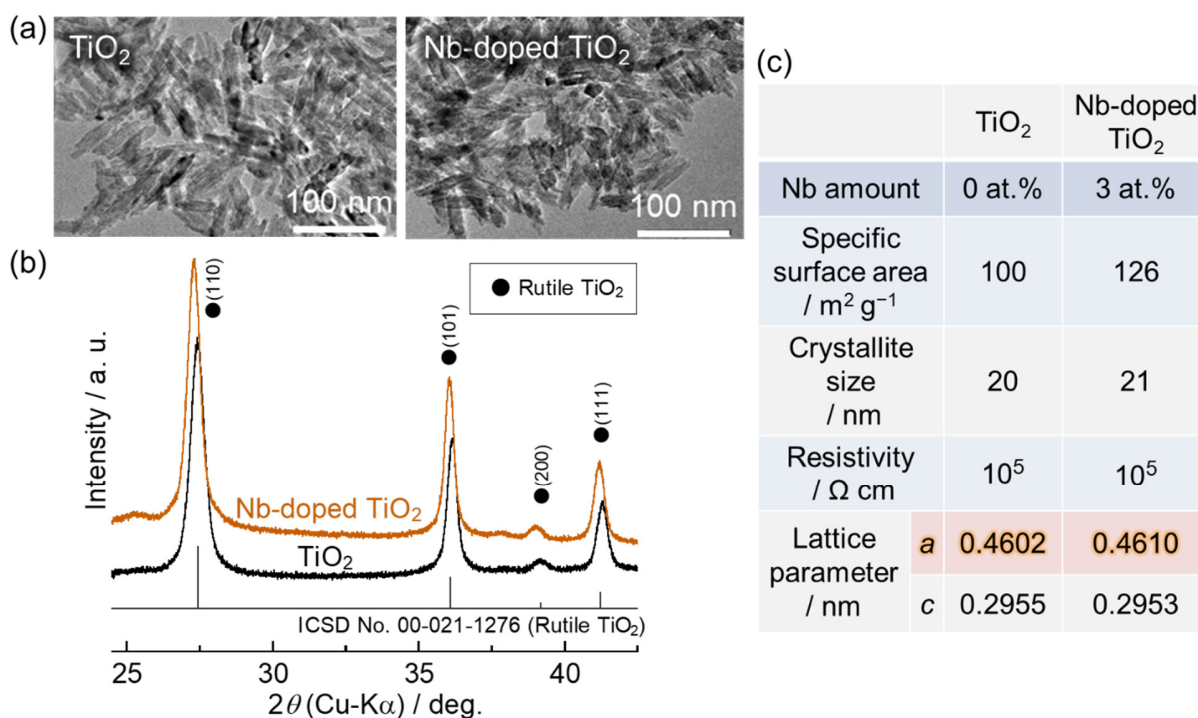


**Figure S10** (a) TEM images and (b) XRD patterns of undoped and Nb-doped spindle TiO<sub>2</sub> particles synthesized by the mass-production sulfate process. (a) Summary of the material characterization. The Nb-doping amount was confirmed by an X-ray fluorescent analysis. The electrical resistivities were measured for pressed powder.

The initial Coulombic efficiency was improved from 73% to 82% by Nb doping (**Figure S11(a)**). It is suggested that the partial pulverization at the initial cycle was relatively suppressed because the Nb-doped  $\text{TiO}_2$  has a larger size of the  $\text{Li}^+$  diffusion path. The authors tried to further improve the efficiency by increasing the cut-off potential from 1.0 to 1.2 V vs.  $\text{Li}^+/\text{Li}$  (**Figure S11(b)**). As a result, the efficiency could be improved from 82% to 88%, whereas the reversible capacity was decreased to  $147 \text{ mA h g}^{-1}$ . In the initial 30 cycles, the spindle Nb-doped  $\text{TiO}_2$  electrode exhibited higher discharge capacities compared with the spindle undoped  $\text{TiO}_2$  electrode (**Figure S11(c)**). However, the capacity fading was observed for the Nb-doped  $\text{TiO}_2$  electrode after the third cycle. After a long period of cycling, the capacity was comparable to that of undoped  $\text{TiO}_2$  electrode.

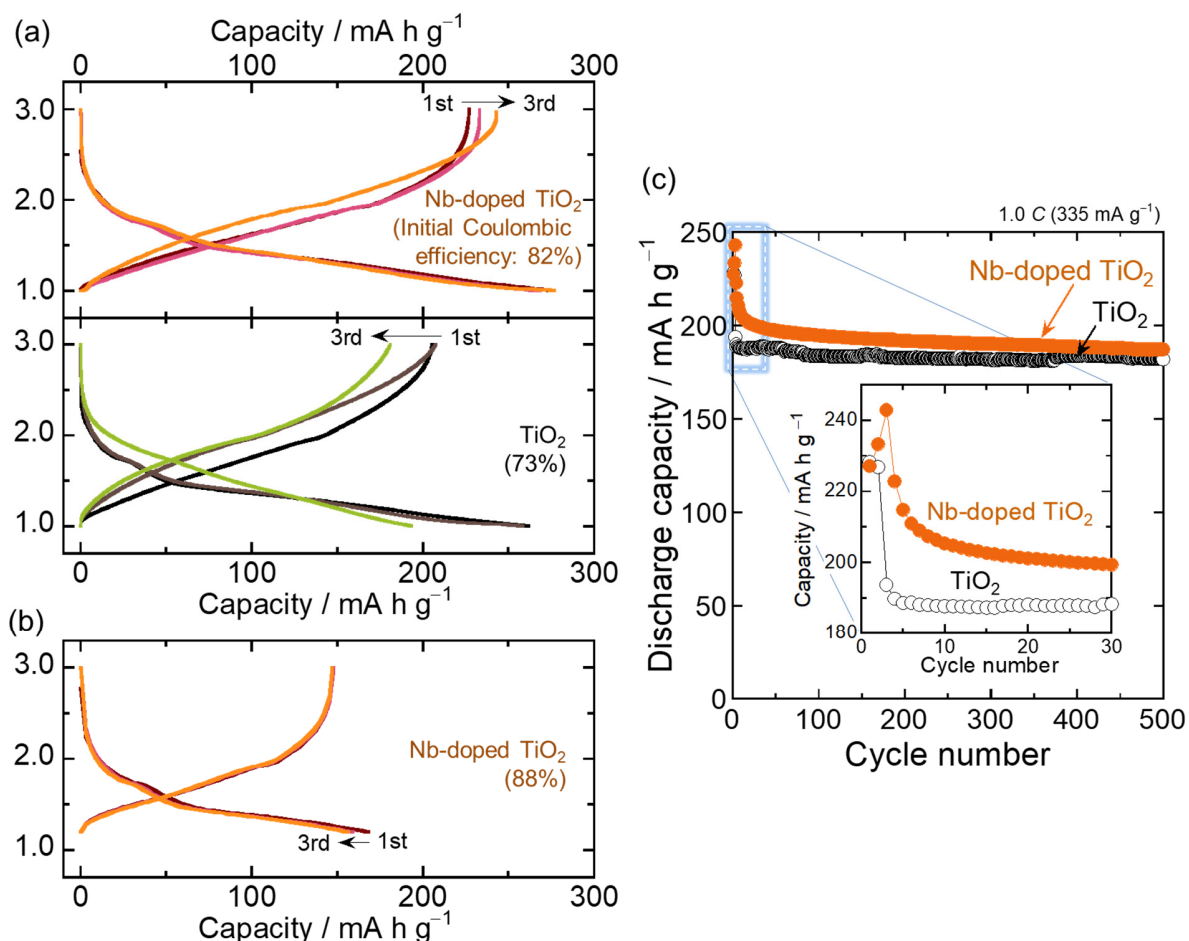


**Figure S11** (a) Constant-current charge–discharge curves of the Nb-doped spindle  $\text{TiO}_2$  electrode in the initial three cycles under current density of  $335 \text{ mA g}^{-1}$  ( $1.0 \text{ C}$ ) with potential ranges of (a)  $1.0\text{--}3.0$  and (b)  $1.2\text{--}3.0$  V vs.  $\text{Li}^+/\text{Li}$ . (c) Cycling performance of the Nb-doped  $\text{TiO}_2$  electrode with potential range of  $1.0\text{--}3.0$  V vs.  $\text{Li}^+/\text{Li}$ .

The benefits of rutile structure and Nb doping were more obviously obtained in rate capability tests (**Figure S12**). At low  $C$  rates less than  $2.0\ C$  ( $0.67\ \text{mA g}^{-1}$ ), the nano-anatase  $\text{TiO}_2$  electrode showed higher discharge capacities. This is due to a much larger specific surface area of  $313\ \text{m}^2\ \text{g}^{-1}$  for the nano-anatase particles.  $\text{Li}^+$ -insertion–extraction reactions can be enhanced by the larger contact area between the particle surface and the electrolyte. In contrast, at the high  $C$  rates larger than  $5.0\ C$  ( $1.68\ \text{mA g}^{-1}$ ), the capacities of the spindle undoped rutile electrode were higher than those of the nano-anatase electrode. It is suggested that the fast  $\text{Li}^+$  kinetics in rutile  $\text{TiO}_2$  probably contributes to the better anode performance at the higher  $C$  rates. When Nb was doped into rutile  $\text{TiO}_2$ , a further improvement in the rate performance could be attained because of the enlarged size in the  $\text{Li}^+$  diffusion path. With increasing  $C$  rate, the superiority of performance of the spindle Nb-doped  $\text{TiO}_2$  electrode became clearer. Even at a high rate of  $20\ C$ , the capacity of  $114\ \text{mA h g}^{-1}$  was attained, which is large than that of  $85\ \text{mA h g}^{-1}$  for the undoped one. This high-rate performance is superior to those of  $\text{TiNb}_2\text{O}_7$  electrode of  $105\ \text{mA h g}^{-1}$  at  $4\ C$  (Han, J. T. *et al.*, *Chem. Mater.* **2011**, 23, 2027.), anatase  $\text{TiO}_2$  electrode of  $75\ \text{mA h g}^{-1}$  at  $10\ C$  (Søndergaard, M. *et al.*, *Chem. Mater.* **2015**, 27, 119.),  $\text{TiO}_2(\text{B})$  electrode of  $110\ \text{mA h g}^{-1}$  at  $10\ C$  (Beuvier, T. *et al.*, *Inorg. Chem.* **2010**, 49, 8457.), and Sn-doped rutile  $\text{TiO}_2$  electrode of  $100\ \text{mA h g}^{-1}$  at  $6\ C$  (Lübke, M. *et al.*, *Electrochim. Acta* **2017**, 231, 247.). On the other hand, a good rate capability of  $96\ \text{mA h g}^{-1}$  at  $40\ C$  has been achieved for Nb-doped rutile electrode (Lan, T. *et al.*, *Chem. Eur. J.* **2017**, 23, 5059.). It is suggested that Nb doping into rutile is very effective for enhancing its rate capability.

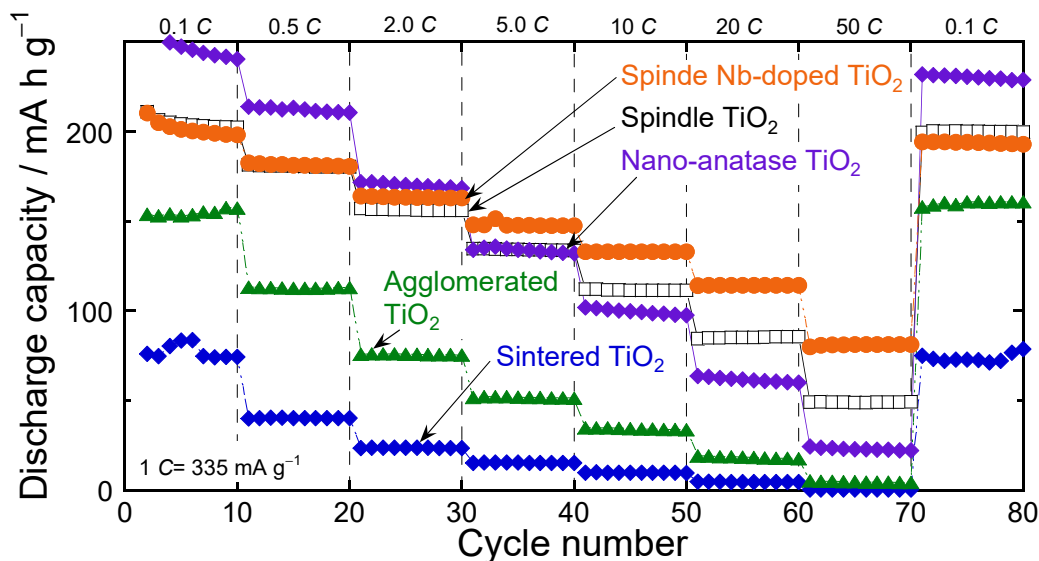


**Figure S12** Rate capability of the spindle Nb-doped  $\text{TiO}_2$  electrode evaluated under the current density from  $33.5\ \text{mA g}^{-1}$  ( $0.1\ C$ ) to  $16.75\ \text{A g}^{-1}$  ( $50\ C$ ). For comparison, the results of nano-anatase  $\text{TiO}_2$  electrode and sintered  $\text{TiO}_2$  electrode were also shown.

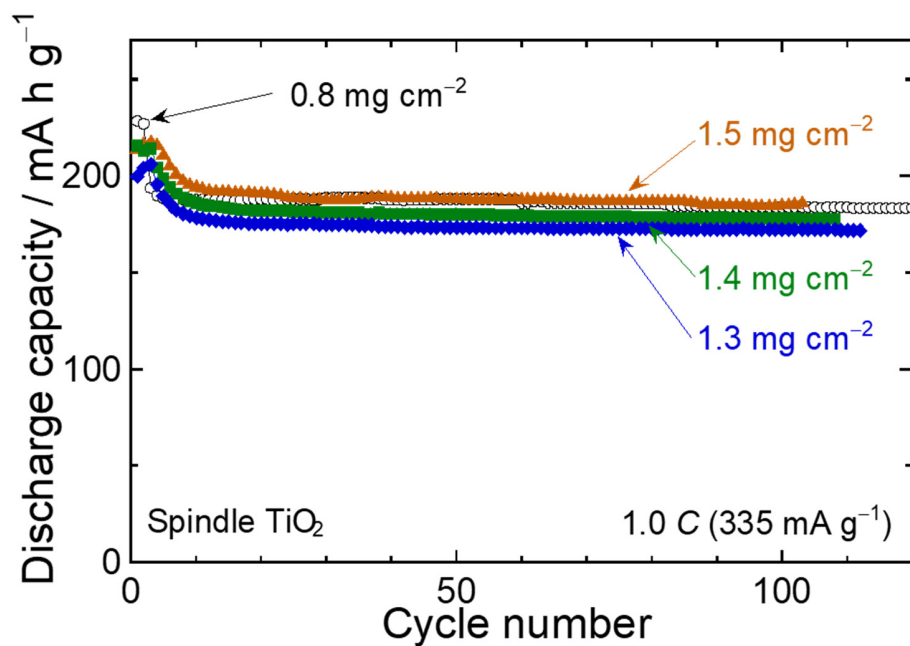


**Figure S13** Cycling performances of spindle rutile  $\text{TiO}_2$  electrodes with thicker coverages of 1.3–1.5  $\text{mg cm}^{-2}$ . Although the coverage of 0.8  $\text{mg cm}^{-2}$  was relatively low, comparable performances were obtained for the thicker coverages. This result demonstrated that spindle  $\text{TiO}_2$  can exhibit good anode properties even when the coverage is increased up to 1.5  $\text{mg cm}^{-2}$ .